

1 **An idealized semi-empirical framework for modeling the**
2 **Madden-Julian oscillation**

3 ADAM SOBEL *

Department of Applied Physics and Applied Mathematics, Department of Earth and Environmental Sciences, and

Lamont-Doherty Earth Observatory, Columbia University, New York, NY

4 ERIC MALONEY

Department of Atmospheric Science, Colorado State University, Fort Collins, Colorado

* *Corresponding author address:* Columbia University, Dept. of Applied Physics and Applied Mathematics, 500 W. 120th St., Rm. 217, New York, NY 10027 USA.

E-mail: latex@ahs129@columbia.edu

ABSTRACT

5
6 We present a simple semi-empirical model to explore the hypothesis that the Madden-Julian
7 oscillation can be represented as a moisture mode destabilized by surface flux and cloud-
8 radiative feedbacks. The model is one-dimensional in longitude; vertical and meridional
9 structure are entirely implicit. The only prognostic variable is column water vapor, W . The
10 zonal wind field is an instantaneous, diagnostic function of the precipitation field.

11 The linearized version of the model has only westward-propagating (relative to the mean
12 flow) unstable modes, because wind-induced surface latent heat flux anomalies occur to the
13 west of precipitation anomalies. The maximum growth rate occurs at the wavelength at
14 which the correlation between precipitation and surface latent heat flux is maximized. This
15 wavelength lies in the synoptic- to planetary-scale range and is proportional to the horizontal
16 scale associated with the assumed diagnostic wind response to precipitation anomalies.

17 The nonlinear version of the model has behavior that can be qualitatively different from
18 the linear modes, and is strongly influenced by horizontal advection of moisture. The non-
19 linear solutions are very sensitive to small shifts in the phasing of wind and precipitation.
20 Under some circumstances nonlinear eastward-propagating disturbances emerge on a state
21 of mean background westerlies. These disturbances have a shock-like discontinuous jump
22 in humidity and rainfall at the leading edge; humidity decreases linearly and precipitation
23 decreases exponentially to the west.

1. Introduction

We propose a highly idealized model of intraseasonal disturbances. The model is motivated by a desire to understand the Madden-Julian oscillation (MJO; Madden and Julian 1971). The degree to which the model in its current form it is relevant to the observed MJO is unclear. We view it as a straightforward extension of certain even simpler models, in a direction of increasing fidelity to the realities of the MJO. The model makes a number of strong simplifying assumptions, motivated by observations, theory, and particularly recent numerical modeling (e.g., Maloney et al. 2010), which embody a set of hypotheses about the dynamics of the MJO. Constructing a simple model based on these hypotheses is one way of testing them; if the model cannot produce an MJO-like disturbance within a reasonable parameter range, it is an indication that one or more of the hypotheses needs revision. The hypotheses are:

- i. The MJO is a "moisture mode", meaning that it depends essentially on a prognostic humidity equation and is not analogous to any dynamical mode which occurs in a dry atmosphere. Moisture modes (sometimes called by other names) have been studied previously in many other models with varying degrees of complexity (Neelin and Yu 1994; Sobel et al. 2001; Fuchs and Raymond 2002, 2005, 2007; Sobel and Bretherton 2003; Raymond and Fuchs 2009; Sugiyama 2009a,b; Majda and Stechmann 2009; Maloney et al. 2010; Kuang 2011; Andersen and Kuang 2011). Growth of such disturbances is governed by feedbacks that increase moisture anomalies, and their propagation is governed by processes that make moisture anomalies move horizontally. Horizontal moisture advection in particular may be important (e.g., Maloney et al. 2010). According to this hypothesis, the MJO is not a Kelvin wave; Kelvin waves may play a role in its dynamics, but the MJO does not propagate by interactions between buoyancy and pressure gradients as a Kelvin wave does. It may be that the phenomenon known as the MJO consists of two dynamically different disturbances, a slower-moving one

50 in the Indian and western Pacific basins which is distinct from convectively coupled
51 Kelvin waves (Wheeler and Kiladis 1999; Kiladis et al. 2009), and a faster-moving
52 one in the central and eastern Pacific and Atlantic basins which is essentially Kelvin
53 wave-like. We are interested in the former, non-Kelvin wave-like one.

54 ii. Thermodynamic feedbacks are important energy sources for the MJO. We refer specif-
55 ically to feedbacks between MJO disturbances and the sources and sinks of column-
56 integrated moist static energy, namely surface turbulent fluxes (Emanuel 1987; Neelin
57 et al. 1987) and radiative cooling (Raymond 2000; Fuchs and Raymond 2002). Evi-
58 dence that these feedbacks are important to the MJO comes from both observations
59 and numerical model studies, and is reviewed by Sobel et al. (2008, 2010). Negative
60 gross moist stability has also been proposed as an important contributor to the moist
61 static energy budget of the MJO (Raymond and Fuchs 2009; Raymond et al. 2009).
62 This is not explored directly here, but could be by a straightforward extension of the
63 model.

64 iii. Both vertical and meridional structure can be taken implicit. Our model has only a
65 single prognostic PDE in longitude and time. The prognostic variable is total column
66 water vapor. We assume that the meridional and vertical structures are known and
67 that the processes that determine them can be taken for granted. This could be argued
68 more formally by projection on a set of basis functions, in the meridional (Majda and
69 Khouider 2001) or vertical (e.g., Neelin and Zeng 2000). While our single prognostic
70 variable would be formally consistent with a single basis function in the vertical, some
71 key effects of variable structure can nonetheless be captured implicitly by extensions of
72 the model presented here that do not require changing its basic form. For example, the
73 effect of variable vertical structure on gross moist stability (e.g., Haertel et al. 2008)
74 might be represented by a parameterization of the gross moist stability as a function
75 of humidity or zonal wind.

76 iv. Convection in the MJO is in a state of quasi-equilibrium with its forcings. We assume
77 that the precipitation and convective heating can at any moment be taken to be an
78 instantaneous function of the thermodynamic state.

79 v. Large-scale wind anomalies associated with the MJO can be taken to be a quasi-steady
80 response to heating. That is, the wind field can be diagnosed instantaneously from the
81 heating field at a given moment. This amounts to an assumption that the time scale
82 for the steady response to a fixed heat source to be established is short compared to
83 the MJO frequency. This assumption allows a strong simplification of the model. It
84 is suggested by observational studies showing a broadly Gill (1980) - type structure to
85 MJO wind anomalies (e.g., Chen et al. 1996), and is shown explicitly to be the case
86 in an idealized numerical model by Sugiyama (2009b). A plausible structure of the
87 wind response to heating is specified in this work based on the Gill model, but we view
88 the more precise definition of this structure as a target for future study. Processes not
89 explicitly included, such as convective momentum transport (e.g., Houze et al. 2000;
90 Tung and Yanai 2000a, b; Lin et al. 2004; Miyakawa et al. 2011), could be included
91 implicitly by their influence on the projection operator which relates wind to heating.
92 The model behavior is sensitive to details of this assumed wind structure.

93 vi. Ocean coupling is not essential. A large number of GCM studies indicate that while
94 ocean coupling may improve the simulation of the MJO, it is not essential to the
95 existence of the MJO (Waliser et al. 1999; Hendon 2000; Kemball-Cook et al. 2002;
96 Inness and Slingo 2003; Zheng et al. 2004; Maloney and Sobel 2004; Grabowski 2006; Fu
97 et al. 2007). The essential mechanisms of MJO development, maintenance, propagation
98 and scale selection should operate in an uncoupled context. Ocean coupling can be
99 straightforwardly added to the present model, but we do not do so here.

100 In section 2 we introduce the model. In section 3 we linearize the model and show the
101 properties of its linear normal modes. In section 4 we present a few representative numerical

102 solutions of the fully nonlinear model, and in section 5 we conclude.

103 2. Model framework

104 a. Basic equations

105 The only prognostic equation for the atmosphere in our model is one for column-integrated
106 water vapor, $W(x, t)$:

$$\frac{dW}{dt} - M_q \Delta = E - P + k_W \frac{\partial^2 W}{\partial x^2}, \quad (1)$$

107 where d/dt is a material derivative following the zonal flow (discussed further below); E is
108 surface evaporation and P precipitation; and M_q is a gross moisture stratification (Neelin
109 1997) which is the proportionality coefficient relating the column-integrated moisture con-
110 vergence to the upper-level mass divergence, Δ , associated with the baroclinic flow. The
111 last term is zonal diffusion with constant diffusivity k_W . The dry static energy equation is
112 made diagnostic by the weak temperature gradient (WTG) approximation:

$$M_s \Delta = P - R, \quad (2)$$

113 where M_s is the gross dry stability and R is vertically integrated radiative cooling. We have
114 neglected the surface sensible heat flux — a good approximation over tropical oceans — and
115 consistent with the assumption that horizontal temperature gradients are small, neglected
116 horizontal diffusion of dry static energy. The WTG approximation need not rule out all
117 effects of temperature variations; those which are correlated with moisture variations can
118 be included implicitly. The dynamics of gravity and Kelvin wave propagation, on the other
119 hand, are excluded. Adding (1) and (2) gives the moist static energy equation:

$$\frac{dW}{dt} = -\Delta M + E - R + k_W \frac{\partial^2 W}{\partial x^2}, \quad (3)$$

120 where $M = M_s - M_q$ is the gross moist stability (Neelin and Held 1987; Neelin 1997).
121 Eliminating the divergence using (2) in (3), and expanding the total derivative on the LHS

122 gives

$$\frac{dW}{dt} = \frac{\partial W}{\partial t} + u \frac{\partial W}{\partial x} = -\tilde{M}P + E - (1 - \tilde{M})R + k_W \frac{\partial^2 W}{\partial x^2}, \quad (4)$$

123 where $u(x, t)$ is an advecting zonal wind at a nominal steering level, and $\tilde{M} = M/M_s$ is
 124 the "normalized gross moist stability" (defined slightly differently than in Raymond et al.
 125 (2009), in that those authors normalize by moisture convergence rather than dry static
 126 energy divergence).

127 *b. Time and zonal mean budgets*

128 Our model domain represents a longitudinal section through a domain with implicit
 129 latitudinal structure; we solve (4) on $0 < x < L_{max}$, with periodic boundary conditions and
 130 $L_{max} = 40000$ km. We do not assume, however, that the flow lies fully in the zonal plane
 131 with zero meridional component, and accordingly *we do not require that* $\Delta = -\partial u / \partial x$.
 132 Thus the mass, energy, and moisture budgets do not close in the domain integral. They
 133 are in weak temperature gradient balance with an implicit mean meridional (i.e., Hadley)
 134 circulation. In the special case in which time dependence, horizontal advection and diffusion
 135 are all negligible, the precipitation at any x is given by the single-column local expression

$$P = \tilde{M}^{-1}[E - (1 - \tilde{M})R]. \quad (5)$$

136 While advection in particular is generally not negligible, (5) is nonetheless useful in under-
 137 standing some basic properties of the model, as discussed further below. In the general case,
 138 integrating (4) over the domain in x gives

$$\frac{\partial}{\partial t} \int W dx = \int [-\tilde{M}P + E - (1 - \tilde{M})R - u \frac{\partial W}{\partial x} + k_W \frac{\partial^2 W}{\partial x^2}] dx. \quad (6)$$

139 In steady state, the precipitation satisfies

$$\int \tilde{M}P dx = \int [E - (1 - \tilde{M})R - u \frac{\partial W}{\partial x} + k_W \frac{\partial^2 W}{\partial x^2}] dx. \quad (7)$$

140 This equation does not give a closed relationship between domain-averaged quantities; for
 141 example, even if E and R are specified and \tilde{M} is taken constant, computation of the advection

142 term requires knowledge of the longitudinal structure of u and W . Because Δ and u are
143 not uniquely related, the explicit horizontal advective transport can have a nonzero domain
144 average and it is not helpful to phrase the model in flux form. Equation (7) simply shows the
145 nature of the local zonal mean WTG balance. While there are implicit latitudinal transports,
146 at this stage we do not explicitly model latitudinal transports associated with meridional
147 gradients — there are no advective or diffusive terms involving derivatives of W with respect
148 to latitude. Such terms may under some circumstances be quantitatively non-negligible, and
149 could be added in parameterized form.

150 Taking the zonal wind u to advect the entire column water vapor, as in (4), may overes-
151 timate the effect of horizontal advection. Horizontal advection of moisture has been shown to
152 be greatest in the lower free troposphere in observations (Benedict and Randall 2007) and
153 simulations (e.g., Maloney 2009; Maloney et al. 2010), but the zonal wind tends to change
154 sign with height in MJO events while the moisture gradient generally does not. In the
155 quasi-equilibrium tropical circulation model (QTCM), for example (Neelin and Zeng 2000;
156 Zeng et al. 2000), the horizontal advection term computed from explicit projection on the
157 assumed vertical structures is multiplied by a coefficient on the order of 0.3 to capture this.
158 On the other hand, the lower tropospheric water vapor is presumably the more important
159 for controlling convection while the upper tropospheric water vapor is expected to vary more
160 as a passive response to convection (e.g., Sherwood 1999; Sobel et al. 2004), so one could
161 argue that for the model to capture that feedback it should weight lower-level advection
162 more heavily.

163 *c. Model physics*

164 Our convective closure models P as a function of W , $P = P(W)$. The relationship
165 between precipitation and column water vapor is the subject of both theoretical and obser-
166 vational work (Raymond 2000; Bretherton et al. 2004; Peters and Neelin 2006; Neelin et
167 al. 2009; Muller et al. 2009), and it has been suggested that the simulation of the MJO

168 in global models is sensitive to it (Benedict and Randall 2009; Zhu et al. 2009). Here, we
 169 choose $P(W)$ according to the observational study of Bretherton et al. (2004):

$$P = P_R \exp[a_d F], \quad (8)$$

170 with $a_d = 15.6$, $P_R = 8.22 \times 10^{-5} \text{mm d}^{-1}$, and F the saturation fraction

$$F = \frac{W}{W_{max}}, \quad (9)$$

171 with W_{max} the saturation column water vapor. [The expression (8) is equivalent to that used
 172 by Bretherton et al. (2004) with the equivalence $P_R = \exp(-a_d r_d)$, $r_d = 0.603$.] Here W_{max}
 173 is chosen to be 70 mm, consistent with typical warm pool values.

174 We parameterize atmospheric radiative cooling by a clear-sky term, taken constant, plus
 175 a cloud-radiative feedback term taken proportional to precipitation, with the additional
 176 requirement that the net effect of radiation must be to cool, not heat the atmosphere:

$$R = \max(R_0 - rP, 0). \quad (10)$$

177 We expect that this radiative feedback will be destabilizing and assist in the development and
 178 maintenance of intraseasonal disturbances (e.g., Raymond 2001, Sobel and Gildor 2003, Bony
 179 and Emanuel 2005; Zurovac-Jevtic et al. 2006; Sobel et al. 2008, 2010, Andersen and Kuang
 180 2011, Landu and Maloney 2011). Bretherton and Sobel (2002) estimated $r \approx 0.15 - 0.2$
 181 from observations, depending on the data set used. Lin and Mapes (2004) performed a more
 182 thorough study with a broader range of data sets and estimated $r \approx 0.1 - 0.15$. Our control
 183 value is $r = 0.1$, at the low end of this range; sensitivity of the model to r is discussed below.

184 Surface evaporation is parameterized as a function of steering level wind speed:

$$E = E_0 + C_u |u|. \quad (11)$$

185 The dependence on wind speed is motivated by results from the simulation of Maloney et al.
 186 (2010). Figure 1 shows daily mean values of surface latent heat flux and 850 hPa zonal wind
 187 from the simulation described in that study; values shown in Fig. 1 are taken only from

188 the warm pool region where the simulated MJO disturbances are most active. While the
189 latent heat flux in these simulations does depend on an air-sea humidity difference according
190 to a standard bulk formula, to first order the wind speed at 850 hPa appears to contain
191 sufficient information to compute the flux. Parameterizing E as a function of $|u|$ but not W
192 allows us to avoid representing the surface air humidity as a function of column water vapor,
193 something that is difficult to do well without an explicit boundary layer. Plots analogous
194 to Fig. 1 made from observed data or reanalyses show greater scatter than does Fig. 1, but
195 similar regression slopes (not shown). The linear regression line in Fig. 1 implies parameter
196 choices $E_0 = 99.9 \text{ W m}^{-2}$, $C_u = 7.9 \text{ W m}^{-3} \text{ s}$; we use $E_0 = 100 \text{ W m}^{-2}$, $C_u = 7.5 \text{ W m}^{-3} \text{ s}$
197 as our control values.

198 The normalized gross moist stability, \tilde{M} , is taken constant and positive in this study.
199 Variable \tilde{M} can be included, and most obviously could be parameterized as a function of W
200 (such dependence would be required to write a closed moisture budget in flux form in the
201 zonal plane, but as discussed above our system is open, with implicit meridional transport).

202 With the radiative parameterization (10), if P remains smaller than $R_0 r^{-1}$, the precip-
203 itation in steady state for the special case of negligible horizontal advection and diffusion,
204 (5), can be written

$$\tilde{M}_{eff} P = E - (1 - \tilde{M}) R_0, \quad (12)$$

205 where $\tilde{M}_{eff} = \tilde{M}(1+r) - r$ is a normalized "effective gross moist stability" including radiative
206 feedbacks (e.g., Bretherton and Sobel 2002; Su and Neelin 2002). For our control parameters,
207 $M_{eff} = 0.01$, while E and $(1 - \tilde{M})R_0$ are typically close in value. Thus the steady state
208 precipitation in this idealized case results from a delicate balance in the moist static energy
209 budget in which the forcing and effective gross moist stability are both small. Our actual
210 solutions (in the nonlinear regime) are in general strongly influenced by horizontal advection,
211 so that in statistically steady state they obey (7) in the domain average rather than the
212 simpler (12), but M_{eff} and $E - (1 - \tilde{M})R_0$ remain important quantities for the control of
213 the mean state. As the zonal mean surface evaporation E is strongly controlled by the wind

214 and thus the amplitude of propagating disturbances, the disturbances and mean state are
 215 in general coupled whether horizontal advection is important or not. Tuning is required to
 216 keep the mean precipitation close to values observed in earth’s tropics. While this is not
 217 in principle a desirable feature, it appears to be broadly consistent with observations which
 218 show that the gross moist stability (and by implication the effective gross moist stability as
 219 well) is not clearly distinguishable from zero in the rainiest parts of the tropics (Back and
 220 Bretherton 2006).

221 *d. Zonal wind as a diagnostic function of precipitation*

222 We impose a constant background wind, U , such that $u(x, t) = U + \hat{u}(x, t)$. We do this
 223 even in the nonlinear model, though the hat is used in section 3 to denote linear perturbations
 224 in other quantities as well as u . The constant background wind reflects the influence of
 225 implied Hadley and Walker circulations unresolved by our model. The perturbation $\hat{u}(x, t)$
 226 need not have zero mean in general. If Δ were proportional to $\partial u / \partial x$, as in idealized ”mock
 227 Walker” models (e.g., Bretherton and Sobel 2002) we could simply integrate Δ to find
 228 \hat{u} . Instead we assume that \hat{u} is both divergent and rotational, but that it can be computed
 229 instantaneously from the total atmospheric heating, $P - R$, via a projection operator, similar
 230 to a Green’s function:

$$\hat{u}(x, t) = \int G(x|x')(P(x', t) - R(x', t))dx'. \quad (13)$$

231 We can determine G empirically or theoretically. Here, we derive G from the solutions of Gill
 232 (1980) to the linear shallow water system on an equatorial beta plane subject to a localized
 233 mass source forcing and Rayleigh damping on the mass and momentum fields, but also allow
 234 an ad hoc zonal shift of the wind response, δ , relative to the heating:

$$G(x|x') = -Ae^{-[x-(x'+\delta)]/L}, \quad x > x' + \delta, \quad (14)$$

$$G(x|x') = 3Ae^{3[x-(x'+\delta)]/L}, \quad x < x' + \delta. \quad (15)$$

235 with A and L constants. For $\delta = 0$, this can be derived from Gill's model in the equatorially
236 symmetric case if the heating has the meridional structure assumed by Gill, but is a delta
237 function in longitude. The length scale L can be interpreted as the group velocity of free
238 Kelvin waves (for $x > x'$) or Rossby waves (for $x < x'$) divided by the Rayleigh damping
239 rate (e.g., Sarachik and Cane 2010, pp. 157-162). The factor of 3 expresses the fact that the
240 group velocity of Kelvin waves is three times that of long Rossby waves. Use of a Gill solution
241 for an off-equatorial forcing strengthens the westerly component relative to the easterly (if
242 the near-equatorial wind is still taken to be the relevant one) but does not significantly shift
243 the relative longitudinal position of the peak westerlies. Sensitivity of the model behavior
244 to this change, and other plausible variations in G , will be addressed in future work.

245 In this study we choose the length scale L to be 1500 km. This is consistent with an
246 equivalent depth of 40m (Kelvin wave speed 20 m s^{-1}) if the dissipation time scale for the
247 wave response to heating is 1d, characteristic of boundary layer drag (arguably appropriate
248 for surface wind, though too small for free-tropospheric wind). The value 40m is slightly
249 higher than that found by Wheeler and Kiladis (1999) for convectively coupled waves, but
250 considerably smaller than would be appropriate for dry equatorial waves. While there is a
251 temperature and wind response that propagates at around 40 m s^{-1} (Bantzer and Wallace
252 1996), the convective signal does not propagate this quickly. Our value of 20 m s^{-1} is
253 consistent with the speed found in observations by Maloney and Shaman (2008) for the
254 observed propagation of the MJO into the Atlantic, and that found in GCM simulations for
255 the Kelvin wave response to the switch-on of a localized SST anomaly (Maloney and Sobel
256 2007). Sensitivity of our model to L is clear in the linear calculations, below; sensitivity to
257 it in the nonlinear system is deferred to future work.

258 The parameter δ , introduced in Eqs. (14)-(15) is a distance by which the response G is
259 shifted relative to where it would be relative to that obtained from (14)-(15). We adopt this
260 device to allow the transition between easterly and westerly events to depart slightly from
261 what one would expect from the Gill solution. Such departures could result from a number

262 of factors not present in the highly idealized linear shallow water system including more
263 complex vertical structure, convective momentum transport (Houze et al. 2000; Tung and
264 Yanai 2002a,b; Lin et al. 2004; Miyakawa et al. 2011), meridional momentum transport by
265 synoptic-scale disturbances (Biello et al. 2007; Showman and Polvani 2010), or nonlinearity
266 in the direct flow response to MJO-scale heating (Gill and Phillips 1986). These factors might
267 well change the structure of G as well as its phase; such structural changes may be of interest
268 in future studies but are not considered here. We do not argue that any particular value of
269 δ is appropriate to represent reality, but find the sensitivity of the model to this parameter
270 interesting. We do require δ to be relatively small compared to L ; the largest value used in
271 this study is $4L/15$, or $0.27L$. The amplitude A is chosen so that precipitation anomalies
272 of planetary spatial scale have wind anomalies whose magnitude in m s^{-1} is comparable to
273 that of the precipitation anomalies in mm d^{-1} , as occurs in the simulations of Maloney et
274 al. (2010).

275 *e. Summary remarks on model construction*

276 In essence, the present model can be viewed as an extension of a simple WTG single-
277 column model (e.g., Sobel and Gildor 2003; see also Maloney and Sobel 2004) to incorporate
278 one horizontal dimension (longitude). As in such models, the present model's essential dy-
279 namics include those relating moisture and convection under the weak temperature gradient
280 approximation (2), the convective closure (8), and the simple cloud-radiative feedback (10).
281 These processes (in less heavily parameterized form) have been found to cause spontaneous
282 self-aggregation of convection in large-domain cloud resolving simulations (Bretherton et al.
283 2005), behavior which is captured by the existence of multiple equilibria (convecting and
284 non-convecting) in WTG single-column (Sobel et al. 2007) or small-domain cloud-resolving
285 models (Sessions et al. 2010). The key new additions here result from the addition of hori-
286 zontal structure, with horizontal wind modeled as a quasi-steady response to precipitation.
287 This allows horizontal advection and large-scale wind-evaporation (WISHE) feedbacks to be

288 explicitly included.

289 The lack of explicit, self-consistent representation of meridional and vertical structure
290 (basis functions, vertical layers, etc.) results from a conscious choice. We hypothesize
291 that a model of the form above with suitable physics may focus our attention usefully on
292 understanding the roles of the different processes as captured by key bulk parameters —
293 e.g., the gross moist stability \tilde{M} , response of wind to heating via L and δ , etc. — and the
294 magnitudes of the terms necessary to generate MJO-like disturbances at some desired level of
295 realism. We postpone any attempt at determining how the full three-dimensional structure
296 of the primitive equations should best be truncated to achieve a self-consistent representation
297 of those processes in terms of explicit but simple vertical and horizontal structures. It is
298 in this sense that we refer to the model as "semi-empirical". At the same time there is
299 nothing particularly new in the essential thermodynamic equation of the model; essentially
300 the same terms and tunable parameters result, in one form or another, from a variety of
301 vertical truncation schemes used in theoretical tropical meteorology, including a two-level
302 or two-layer model (e.g., Neelin et al. 1987; Wang 1988) or projection on vertical basis
303 functions derived from either a dry vertical structure equation (e.g., Stevens and Lindzen
304 1978) or quasi-equilibrium convective constraints on the temperature profile (e.g., Emanuel
305 1987; Neelin 1997). Any novel aspects here result from the use of a prognostic moisture
306 equation but diagnostic (WTG) temperature equation — the opposite choice being more
307 typical historically — and the diagnostic computation of the wind field.

308 **3. Linear analysis**

309 We linearize the model about a background state W_0 ,

$$W = W_0 + \hat{W}(x, t), \quad (16)$$

310 where the hat indicates a small perturbation; the more standard prime is reserved here for
311 the dummy spatial variable x' used in the spatial projection to obtain \hat{u} . The background

312 state is also assumed to have a uniform zonal wind U , so that (as in the nonlinear model)
 313 the total wind is $U + \hat{u}(x, t)$. The linearized model is

$$\frac{\partial \hat{W}}{\partial t} + U \frac{\partial \hat{W}}{\partial x} = -\tilde{M}\hat{P} + \hat{E} - (1 - \tilde{M})\hat{R} + k_w \frac{\partial^2 \hat{W}}{\partial x^2}, \quad (17)$$

314 We linearize our convective parameterization about the state $W = W_0$, $P = P_0 = P_R \exp[a_d(W_0/W_{max})]$,
 315 thus obtaining

$$\hat{P} = \frac{\hat{W}}{\tau_c}, \quad (18)$$

316 where

$$\tau_c = \frac{W_{max}}{a_d P_0} = (a_d P_R)^{-1} W_{max} \exp[-a_d(W_0/W_{max})]. \quad (19)$$

317 Our linearized radiative perturbations are then

$$\hat{R} = -r\tau_c^{-1}\hat{W}, \quad (20)$$

318 while, if we assume westerly mean winds, our perturbation latent heat flux is

$$\hat{E} = C_u \hat{u}. \quad (21)$$

319 Now assuming sinusoidal perturbations,

$$\hat{W} = \mathcal{W} e^{i(kx - ct)}, \quad (22)$$

320 with \mathcal{W} a complex amplitude and c a (potentially) complex phase speed, and substituting
 321 we obtain

$$ik(U - c)\hat{W} = -[\tau_c^{-1}\tilde{M}_{eff} + k_w k^2]\hat{W} + C_u \hat{u}. \quad (23)$$

322 With a projection function of the form (14)-(15) and using (18) and (20), (13) can be
 323 written

$$\hat{u}(x, t) = \int G(x|x') \hat{P}(x', t) (1 + r) dx' = (1 + r) \tau_c^{-1} \int G(x|x') \hat{W}(x', t) dx'. \quad (24)$$

324 For sinusoidal disturbances as described by (22), \hat{u} can be found analytically,

$$\hat{u} = \Gamma(k) \hat{P} = \Gamma(k) \frac{\hat{W}}{\tau_c}, \quad (25)$$

325 where

$$\Gamma(k) = (1 + r) \left(\frac{4Ae^{-ik\delta} \left[\frac{2k^2}{L} + i \left(\frac{3k}{L^2} + k^3 \right) \right]}{(9/L^2 + k^2)(1/L^2 + k^2)} \right). \quad (26)$$

326 From this it follows that the phase angle, call it α , by which \hat{u} lags \hat{P} is

$$\alpha = \tan^{-1} \left(\frac{3}{2kL} + \frac{kL}{2} \right) - k\delta. \quad (27)$$

327 For $\delta = 0$, the zonal wind and precipitation fields are thus in quadrature ($\alpha = \pi/2$) when
 328 the dimensionless ratio of length scales kL is either zero (long wavelength $2\pi/k$ compared
 329 to wind decay scale L) or infinite (short wavelength). For $\delta = 0$ the wind is most nearly
 330 in phase with precipitation at the value $kL = \sqrt{3}$ at which $\alpha = \tan^{-1} \sqrt{3} = \pi/3$; for δ
 331 small (compared to $\pi/3k$) but nonzero, the minimum phase lag is $\alpha = \pi/3 - k\delta$. The
 332 fact that α differs at all from $\pi/2$ for any finite L is a consequence of the asymmetry of
 333 G , resulting from the different decay scales of the Rossby and Kelvin components. For an
 334 antisymmetric projection function in which the decay scales are the same to the east and west
 335 of the forcing — as would result (for example) in an analog to the Gill model for planetary
 336 vorticity gradient $\beta = 0$, in which only inertia-gravity waves could carry the linear response
 337 to forcing, and would have the same wave speeds to the east or west — u and P will be in
 338 quadrature for any value of that decay scale.

339 The importance of the phase lag between wind and precipitation is apparent if we take
 340 the linear atmospheric equation (17), multiply by \hat{W} , substitute $\hat{P} = \tau_c^{-1} \hat{W}$ and $\hat{R} = -r\hat{P}$,
 341 and integrate over the domain, assumed periodic, to obtain an equation for the variance of
 342 W' :

$$\frac{\partial}{\partial t} \int \frac{1}{2} \hat{W}^2 dx = -\tau_c^{-1} \tilde{M}_{eff} \int \hat{W}^2 dx + \int \hat{E} \hat{W} dx - k_w \int \left(\frac{\partial \hat{W}}{\partial x} \right)^2 dx. \quad (28)$$

343 While (28) assumes a periodic domain, it does not assume sinusoidal perturbations. The last
 344 term on the RHS is negative definite, and the first is as well if M_{eff} is positive. In that case
 345 amplitude growth can result only from the second term, which is the covariance of surface
 346 latent heat flux and column water vapor. Under our assumptions this wind-evaporation
 347 feedback term will be positive in general for a westerly mean state and perturbations whose

348 maximum winds are westerly and lag the precipitation with respect to longitude. These
 349 conditions are fundamentally different from those under which WISHE is destabilizing for a
 350 convectively coupled Kelvin wave destabilized by wind-evaporation feedback in an easterly
 351 flow (Emanuel 1987; Neelin et al. 1987).

352 In this model, as discussed above the existence of a spatial correlation between u and P
 353 results from the east-west asymmetry in G . Since E is assumed proportional to u while P
 354 is proportional to W , (28) thus implies that the destabilizing effect of WISHE in this model
 355 also results from that asymmetry in G . That destabilization is thus a consequence of the
 356 symmetry-breaking effect of the planetary vorticity gradient, β .

357 For the linear system, using (25), (23) becomes

$$ik(U - c)\hat{W} = \tau_c^{-1}[r - \tilde{M}(1 + r) + C_u\Gamma - \tau_c k_w k^2]\hat{W}, \quad (29)$$

358 OR

$$c = U + \frac{\tilde{M}_{eff} - C_u\Gamma + \tau_c k_w k^2}{ik\tau_c}, \quad (30)$$

359 The phase speed c and wind-precipitation proportionality factor Γ are both complex in
 360 general; all other coefficients in (29) are real. The disturbances propagate at a real phase
 361 speed $Re(c)$, while $Im(c)k$ is the linear growth rate. These two quantities are shown in Fig. 2
 362 for the parameters shown in Table 1, except that k_w is set to zero; the value used in the
 363 nonlinear calculations is sufficiently small that including it does not significantly change the
 364 results (not shown). In these calculations the mean state column water vapor is $W_0 = 45$
 365 mm, resulting in a convective time scale $\tau_c = 2.4$ d. The growth rate and phase speed
 366 are both inversely proportional to τ_c , as can be seen from (30). The growth rate has its
 367 maximum at zonal wave number 7.3, or a wavelength of 5440 km, consistent with the value
 368 $kL = \sqrt{3}$ as discussed above. A larger value of the parameter L would of course lead to a
 369 larger wavelength at the maximum growth rate.

370 Figure 3 shows the same calculations for a range of values in the key parameters r and δ .
 371 We see that increasing either parameter increases the growth rate, while the shapes of the
 372 curves remain qualitatively similar as these two parameters are varied

373 Figure 4 shows the sensitivity to the inverse convective time scale, τ_c^{-1} , which grows
374 exponentially with the background moisture W_0 according to (19). The growth rate increases
375 rapidly with τ_c^{-1} , as does the (westward) phase speed. Logarithmic scales are used on the
376 y -axis of both plots. For large τ_c^{-1} (small τ_c ; the smallest value shown is 0.03 d) the growth
377 rates are so large that nonlinearity would rapidly become important, and the phase speeds
378 are also so large as to render key assumptions of the model (e.g., quasi-stationarity of wind
379 response to heating) invalid.

380 In these linear solutions it is clear why the wind-evaporation feedback (or WISHE) is
381 destabilizing, and how this mechanism controls scale selection in a configuration similar to
382 that of the real MJO where the mean low-level wind is westerly and the largest low-level
383 winds are westerlies occurring to the west of precipitation maxima. At the same time these
384 solutions do not appear explain the propagation dynamics of the MJO at all. They predict
385 only westward phase propagation relative to the basic flow, with phase speeds comparable to
386 or greater than that of typical warm pool low-level mean westerlies so that ground-relative
387 westward propagation, or at best stationarity, is implied. It is possible that these solutions
388 may have some relevance to the dynamics of westward-propagating intraseasonal variability
389 (e.g., Murakami 1980; Kemball-Cook and Wang 2001). Some of this is associated with
390 convectively coupled equatorial Rossby waves (e.g., Kiladis and Wheeler 1995; Wheeler and
391 Kiladis 1999) which may at times interact with the MJO (Roundy and Frank 2004).

392 4. Nonlinear numerical solutions

393 *a. Numerical model configuration and parameters*

394 We solve the nonlinear system numerically on a periodic domain of length 40,000 km, with
395 1000 grid points so the horizontal grid spacing is 40 km. We use a first-order upwind scheme
396 for horizontal advection and a leapfrog time stepping procedure with a Robert-Asselin filter
397 and a time step of 0.001 days. Simulations are initialized somewhat arbitrarily with the

398 initial condition

$$W = W_0 + \Delta W \sin\left(\frac{\pi x}{L_m}\right),$$

399 where here $W_0 = 50\text{mm}$, $\Delta W = 2\text{mm}$, and $L_m = 40000\text{km}$ is the domain size. It is found
400 through experimentation that the qualitative results of interest are not sensitive to the initial
401 conditions, though our exploration of the initial conditions is not at all exhaustive.

402 We impose a background westerly wind of 5 m s^{-1} . This influences both horizontal
403 advection and surface fluxes. We imagine that our domain, despite having an extent ap-
404 proximately equal to the circumference of the earth, consists solely of a "warm pool", or
405 region of relatively high sea surface temperature, while elsewhere (at both other latitudes
406 and longitudes, though neither are explicitly included) the SST is lower. Thus precipitation
407 is focused on the warm pool, and the quasi-steady response includes low-level westerly winds,
408 as is the case in the tropical Indian and western Pacific oceans on earth.

409 *b. Results*

410 Fig. 5 shows Hovmoeller plots of saturation fraction from calculations with parameters
411 shown in table 1 and $\delta = +400, 0,$ and -400 km . Results are shown for periods of 160
412 days; in each case the period shown starts on day 321 of each integration (labeled as day 1
413 in the figure). By this time, initial transient features have decayed leaving nearly periodic
414 disturbances which are close to steady in their respective co-moving reference frames. The
415 first two show eastward propagation, while the third shows westward propagation. In the
416 $\delta = 400 \text{ km}$ solution in the left panel, the eastward propagation speed is close to but less than
417 (i.e., easterly relative to) that of the background wind, 5 m s^{-1} ; the latter value is indicated
418 by the dashed line in the figure. The dominant spatial structures have wave number two for
419 $\delta = 400 \text{ km}$, and wave numbers six and four in the latter two calculations respectively (as
420 made more apparent in the figures below).

421 Figures 6-8 show snapshots of precipitation and perturbation zonal wind (left panels)

422 and water vapor path and surface evaporation (right panels) on day 321 for the same three
 423 calculations shown in Fig. 5, in the same order. Note that the scales on the vertical axes are
 424 not the same for corresponding fields in the different figures. In Fig. 6 we see two isolated
 425 peaks in precipitation, with roughly exponential increases on the western sides and then
 426 step-like decreases back down to a zero background on the eastern sides. This structure
 427 (including the number of peaks, two) appears at least qualitatively independent of initial
 428 conditions, for a range of initial perturbations we have tried (not shown). The zonal wind
 429 has westerlies roughly in phase with precipitation with strong easterlies ahead in the dry
 430 regions. The water vapor path in this solution has a nearly sawtooth wave pattern, with a
 431 linear increase followed by a step decrease. The latent heat flux has two peaks separated
 432 by a sharp minimum at the point where the wind perturbation switches from easterly to
 433 westerly.

434 Fig. 7 shows the same fields as in Fig. 6 but for $\delta = 0$. Recall from Fig. 5 that there is still
 435 some eastward propagation in this solution (also recall that there is a background eastward
 436 wind of 5 m s^{-1}) but the perturbations are smaller in both amplitude and spatial scale than
 437 in Fig. 6. The precipitation features resemble the sharp structures in Fig. 6, but the maxima
 438 are closer together so that the large regions of zero precipitation in Fig. 6 are absent. Close
 439 inspection reveals that E lags W by more than in the previous figure, as expected. These
 440 differences are still more pronounced in Fig. 8, with $\delta = -400 \text{ km}$. Recall from Fig. 5 that
 441 the disturbances in this solution move rapidly westward, despite the eastward basic flow. The
 442 structures in all fields are smoother and closer to sinusoidal than those in figs. 6 and 7. The
 443 precipitation variations, from maximum to minimum, are roughly a factor of three smaller
 444 than those in Fig. 6, while the variations in W are smaller by a factor of five. The lack of
 445 proportionality is due to the exponential convective closure; the solution with $\delta = -400 \text{ km}$
 446 is considerably moister in the mean, resulting in a stronger response to small W variations
 447 (smaller τ_c , in the linearized model).

448 The highly nonlinear solution for positive δ has no analog in the linear system. While

449 simply shifting G as we have done is *ad hoc*, the results demonstrate a strong sensitivity of
450 this system to the phase relationship between zonal wind and precipitation. The existence
451 of these nonlinear solutions depends on both horizontal advection by the perturbation winds
452 (an inherently nonlinear effect) as well as by the mean flow, and on the shifting of E forward
453 so that it is more nearly in phase with W and P (an effect which is present in the linearized
454 model as well). When either of these effects are disabled, the nonlinear mode shown in Fig. 6
455 is strongly weakened or otherwise altered (not shown). An exploration of other parameter
456 choices (not shown) suggests that advection of moisture by the perturbation flow is the
457 more important of the two effects in generating this mode. This is consistent with shock
458 dynamics as found in other systems where an active scalar generates a flow that advects itself
459 in one dimension. While precipitation fronts can also occur in a quasi-linear system without
460 nonlinear horizontal advection (Frierson et al. 2004; Stechmann and Majda 2006; Pauluis
461 et al. 2008), here the role of nonlinear advection is apparent in the correspondence of the
462 front location with that of strong zonal confluence. The effect of this confluence can be seen
463 in the initial $\sim 20 - 30d$ of the left panel in Fig. 5, where eastward- and westward-moving
464 moist regions on either side of $x = 0$ move towards each other before colliding near $x = 0$
465 around $50d$ and coalescing into the narrower structure evident in Fig. 6.

466 While the eastward propagation and planetary horizontal scale of the nonlinear mode
467 might be viewed as encouraging, the discontinuity at the leading edge is not MJO-like.
468 Observations show that the transition from suppressed to active phase is as gradual as that
469 from active back to suppressed, if not more so (Kemball-Cook and Weare 2001; Kiladis
470 et al. 2005; Benedict and Randall 2007). This could indicate that the processes that lead to
471 the slow deepening of convection at the leading edge (e.g., Mapes et al. 2006) need to be
472 represented better in this model. On the other hand it could simply be an indication that
473 the nonlinear mode is an artifact of excessively strong horizontal advection and is irrelevant
474 to the real atmosphere.

475 The model is nonlinear, and many parameter choices affect the mean state as well as the

476 existence or properties of time-dependent perturbations to it. As an example, Fig. 9 shows
 477 an example in which all parameters are the same as in Fig. 6 — in particular, $\delta = 400$ km —
 478 but the cloud-radiative feedback parameter r has been increased from 0.1 to 0.15, rendering
 479 the effective gross moist stability slightly negative, $\tilde{M}_{eff} = -0.035$. The mean state is
 480 dramatically changed, with strong rainfall everywhere and consequently much greater zonal
 481 mean rain rate than in Fig. 6. There are still self-sustained oscillations, but their properties
 482 are quite different from those in Fig. 6. The disturbances move predominantly westward,
 483 and the mean state is quite humid (the same color scale is used as in Fig. 5). Of the solutions
 484 with $r = 0.1$ shown in Fig. 5 the solution looks more similar to that for $\delta = -400$ km than
 485 that for $\delta = +400$ km, though the latter is the value of δ used in Fig. 9.

486 The solution in Fig. 9 illustrates the general property that changes in the perturbations
 487 are generally accompanied by changes in the mean state (though the latter are usually
 488 smaller than those shown here if \tilde{M}_{eff} does not change sign). It is not obvious whether
 489 this property is an advantage or disadvantage for an idealized MJO model. In full-physics
 490 general circulation models, changes in simulated MJO amplitude are also accompanied by
 491 mean state changes (Kim et al. 2011) (though not ones as large as here), and it is possible
 492 that interactions between the seasonal mean circulation and MJO disturbances are important
 493 in the real climate as well. If desired, various devices can be used to constrain the mean
 494 state in the present model, but these will in general also influence the disturbance dynamics.

495 We have performed a wide range of sensitivity studies. Solutions tend to resemble,
 496 qualitatively, one of those in figures 5-9, but a number of parameters influence which type
 497 of solution emerges. Besides δ , r , and \tilde{M} , the saturation column water vapor W_{max} , and
 498 the wind length scale L are also important. We do not present these studies here, as they
 499 are not yet particularly informative. The key result here is the emergence of the strongly
 500 nonlinear solution for positive δ in some parameter regimes. It is clear that this solution does
 501 not emerge for parameters which cause the background state to be very humid and rainy,
 502 as in figs. 8 or 9; such states tend to feature westward-propagating wavelike disturbances

503 whose amplitude in precipitation is modest compared to the mean precipitation (though
504 not necessarily small in absolute terms). The properties of the strongly nonlinear solution
505 appear qualitatively similar in all cases in which it occurs, though there is some variation in
506 the amplitude and spacing between disturbances.

507 **5. Conclusions**

508 We have constructed a one-dimensional semi-empirical framework which we hope may
509 be useful for developing MJO theories. The framework incorporates a number of strong
510 assumptions, but is not based explicitly on a set of pre-defined vertical or meridional struc-
511 tures. This has the disadvantage that internal consistency is not enforced to the degree
512 that it could be, but the advantage that the roles of key parameters or functions can be
513 examined independently, and could in principle be determined based on observations or nu-
514 merical modeling studies. While the particular implementation presented here can, under
515 some circumstances, produce planetary-scale eastward-propagating disturbances when aided
516 by an eastward basic flow, we do not claim at this point that these capture the essential
517 dynamics of the MJO. We believe they capture hypotheses worth exploring, and use them
518 as examples to demonstrate some sensitivities and basic properties of the framework.

519 In the linear regime, unstable normal modes exist but are all westward-propagating
520 relative to the mean flow. Their growth rates and phase speeds are strongly sensitive to
521 the convective time scale, which is a strong function of the mean state humidity. The spatial
522 scale of the fastest growing mode is set by the scale of the quasi-stationary response of the
523 wind to heating, which in reality depends on the effective stratification and damping that
524 act on the forced-dissipative waves that determine that response.

525 In some reasonable parameter regimes, if the projection function G which determines
526 the zonal wind field as a function of precipitation is taken from the equatorially symmetric
527 Gill model but is shifted a few hundred km to the east relative to precipitation, a nonlinear

528 mode emerges which propagates eastward at nearly the speed of the background eastward
529 wind. The disturbances in this mode have a nearly sawtooth structure in humidity and
530 precipitation maxima which decay exponentially westward and with a step function on the
531 eastward side.

532 Extensions of the framework currently under exploration include: variations in the de-
533 terministic convective parameterization $P(W)$; addition of a stochastic component (either
534 additive or multiplicative) to the convective parameterization; variable gross moist stabil-
535 ity, parameterized as a function of column water vapor W or perhaps zonal wind u ; zonal
536 variation in the basic state; explicit (parameterized) representation of meridional advection,
537 including eddy transports which may vary with MJO phase (Maloney 2009; Andersen and
538 Kuang 2011); and coupling to a mixed layer ocean.

539 *Acknowledgments.*

540 This work was supported by NASA grant NNX09AK34G (AHS), NOAA grants NA08OAR4320912
541 (AHS) and NA08OAR4320893 #7 and #14 (EDM), and NSF grants AGS-1008847 (AHS)
542 and AGS-1025584 (EDM). We thank Daehyun Kim for a careful reading of the manuscript.

REFERENCES

- 545 Andersen, J. A. and Z. Kuang, 2011: Moist static energy budget of MJO-like disturbances
546 in the atmosphere of a zonally symmetric aquaplanet. *J. Climate*, submitted.
- 547 Back, L. E. and C. S. Bretherton, 2006: Geographic variability in the export of moist
548 static energy and vertical motion profiles in the tropical Pacific. *Geophys. Res. Lett.*, **33**,
549 doi:10.1029/2006GL026672.
- 550 Bantzer, C. H. and J. M. Wallace, 1996: Intraseasonal variability in tropical mean temper-
551 ature and precipitation and their relation to the tropical 40-50 day oscillation. *J. Atmos.*
552 *Sci.*, **53**, 3032–3045.
- 553 Benedict, J. J. and D. A. Randall, 2007: Observed characteristics of the MJO relative to
554 maximum rainfall. *J. Atmos. Sci.*, **64**, 2332–2354.
- 555 Benedict, J. J. and D. A. Randall, 2009: Structure of the Madden-Julian oscillation in the
556 superparameterized CAM. *J. Atmos. Sci.*, **66**, 3277–3296.
- 557 Biello, J. A., A. J. Majda, and M. W. Moncrieff, 2007: Meridional momentum flux and
558 superrotation in the multiscale IPESD MJO model. *J. Atmos. Sci.*, **64**, 1636–1651.
- 559 Bony, S. and K. A. Emanuel, 2005: On the role of moist processes in tropical intraseasonal
560 variability: Cloud-radiation and moisture-convection feedbacks. *J. Atmos. Sci.*, **62**, 2770–
561 2789.
- 562 Bretherton, C., M. E. Peters, and L. E. Back, 2004: Relationships between water vapor path
563 and precipitation over the tropical oceans. *J. Climate*, **17**, 1517–1528.
- 564 Bretherton, C. S., P. N. Blossey, and M. Khairoutdinov, 2005: An energy-balance analysis
565 of deep convective self-aggregation above uniform SST. *J. Atmos. Sci.*, **62**, 4273–4292.

566 Bretherton, C. S. and A. H. Sobel, 2002: A simple model of a convectively coupled Walker
567 Circulation using the weak temperature gradient approximation. *J. Climate*, **15**, 2907–
568 2920.

569 Chen, S., R. A. Houze Jr., and B. E. Mapes, 1996: Multiscale variability of deep convection
570 in relation to large-scale circulation in TOGA COARE. *J. Atmos. Sci.*, **53**, 1380–1409.

571 Emanuel, K. A., 1987: An air-sea interaction model of intraseasonal oscillations in the
572 tropics. *J. Atmos. Sci.*, **44**, 2324–2340.

573 Frierson, D. M. W., A. J. Majda, and O. Pauluis, 2004: Large scale dynamics of precipitation
574 fronts in the tropical atmosphere: A novel relaxation limit. *Commun. Math. Sci.*, **2**, 591–
575 626.

576 Fu, X., B. Wang, D. E. Waliser, and L. Tao, 2007: Impact of atmosphere-ocean coupling on
577 the predictability of monsoon intraseasonal oscillations. *J. Atmos. Sci.*, **64**, 157–174.

578 Fuchs, Z. and D. J. Raymond, 2002: Large-scale modes of a nonrotating atmosphere with
579 water vapor and cloud-radiation feedbacks. *J. Atmos. Sci.*, **59**, 1669–1679.

580 Fuchs, Z. and D. J. Raymond, 2005: Large-scale modes in a rotating atmosphere with
581 radiative-convective instability and WISHE. *J. Atmos. Sci.*, **62**, 4084–4094.

582 Fuchs, Z. and D. J. Raymond, 2007: A simple, vertically resolved model of tropical distur-
583 bances with a humidity closure. *Tellus*, **59A**, 344–354.

584 Gill, A. E., 1980: Some simple solutions for heat induced tropical circulations. *Quart. J.*
585 *Roy. Meteor. Soc.*, **106**, 447–462.

586 Gill, A. E. and P. J. Phlips, 1986: Nonlinear effects on heat-induced circulation of the tropical
587 atmosphere. *Quart. J. Roy. Meteor. Soc.*, **112**, 69–91.

588 Grabowski, W. W., 2006: Impact of explicit atmosphere-ocean coupling on MJO-like coher-
589 ent structures in idealized aquaplanet simulations. *J. Atmos. Sci.*, **63**, 2289–2306.

590 Haertel, P. T., G. N. Kiladis, A. Denno, and T. M. Rickenback, 2008: Vertical-mode decom-
591 positions of 2-day waves and the Madden-Julian oscillation. *J. Atmos. Sci.*, **65**, 813–833.

592 Hendon, H. H., 2000: Impact of air-sea coupling on the Madden-Julian oscillation in a general
593 circulation model. *J. Atmos. Sci.*, **57**, 3939–3952.

594 Houze Jr., R. A., S. S. Chen, D. E. Kingsmill, Y. Serra, and S. E. Yuter, 2000: Convection
595 over the pacific warm pool in relation to the atmospheric Kelvin-Rossby wave. *J. Atmos.*
596 *Sci.*, **57**, 3058–3089.

597 Inness, P. M. and J. M. Slingo, 2003: Simulation of the Madden-Julian oscillation in a coupled
598 general circulation model. Part I: Comparison with observations and an atmosphere-only
599 GCM. *J. Climate*, **16**, 345–364.

600 Kemball-Cook, S. R. and B. Wang, 2001: Equatorial waves and air-sea interaction in the
601 boreal summer intraseasonal oscillation. *J. Climate*, **14**, 2923–2942.

602 Kemball-Cook, S. R. and B. C. Weare, 2001: The onset of convection in the Madden-Julian
603 Oscillation. *J. Climate*, **14**, 780–793.

604 Kemball-Cook, S., B. Wang, and X. Fu, 2002: Simulation of the intraseasonal oscillation in
605 the ECHAM-4 model: the impact of coupling with an ocean model. *J. Atmos. Sci.*, **59**,
606 1433–1453.

607 Kiladis, G. N. and M. Wheeler, 1995: Horizontal and vertical structure of observed tropo-
608 spheric equatorial Rossby waves. *J. Geophys. Res.*, **100**, 22 981–22 997.

609 Kiladis, G. N., K. H. Straub, and P. T. Haertel, 2005: Zonal and vertical structure of the
610 Madden-Julian oscillation. *J. Atmos. Sci.*, **62**, 2790–2809.

611 Kiladis, G. N., M. C. Wheeler, P. T. Haertel, K. H. Straub, and P. E. Roundy, 2009:
612 Convectively coupled equatorial waves. *Rev. Geophys.*, **47**, doi:10.1029/2008RG000 266.

613 Kim, D., A. H. Sobel, E. D. Maloney, D. M. W. Frierson, and I.-S. Kang, 2011: A systematic
614 relationship between intraseasonal variability and mean state bias in AGCM simulations.
615 *J. Climate*, **24**, 5506-5520.

616 Kuang, Z., 2011: The wavelength dependence of the gross moist stability and the scale
617 selection in the instability of column integrated moist static energy. *J. Atmos. Sci.*, **68**,
618 61–74.

619 Landu, K. and E. D. Maloney, 2011: Understanding intraseasonal variability in an aqua-
620 planet GCM. *J. Meteor. Soc. Japan*, in press.

621 Lin, J. and B. E. Mapes, 2004: Radiation budget of the tropical intraseasonal oscillation. *J.*
622 *Atmos. Sci.*, **61**, 2050–2062.

623 Lin, J., C. Zhang, and B. E. Mapes, 2004: Zonal momentum budget of the Madden-Julian
624 oscillation: The source and strength of equivalent linear damping. *J. Atmos. Sci.*, **62**,
625 2172-2188.

626 Madden, R. A. and P. R. Julian, 1971: Detection of a 40-50 day oscillation in the zonal wind
627 in the tropical Pacific. *J. Atmos. Sci.*, **28**, 702–708.

628 Majda, A. J. and B. Khouider, 2001: A numerical strategy for efficient modeling of the
629 equatorial wave guide. *Proc. Nat. Acad. Sci.*, **98**, 1341–1346.

630 Majda, A. J. and S. N. Stechmann, 2009: The skeleton of tropical intraseasonal oscillations.
631 *Proc. Nat. Acad. Sci.*, **106**, 8417–8422.

632 Maloney, E. D., 2009: The moist static energy budget of a composite tropical intraseasonal
633 oscillation in a climate model. *J. Climate*, **22**, 711–729.

634 Maloney, E. D. and A. H. Sobel, 2004: Surface fluxes and ocean coupling in the tropical
635 intraseasonal oscillation. *J. Climate*, **17**, 4368–4386.

- 636 Maloney, E. D. and A. H. Sobel, 2007: Idealized hot spot experiments with a general circu-
637 lation model. *J. Climate*, **20**, 908–925.
- 638 Maloney, E. D. and J. Shaman, 2008: Intraseasonal variability of the west African monsoon
639 and Atlantic ITCZ. *J. Climate*, **21**, 2898–2918.
- 640 Maloney, E. D., A. H. Sobel, and W. M. Hannah, 2010: Intraseasonal variabil-
641 ity in an aquaplanet general circulation model. *J. Adv. Model Earth Sys.*, **2**,
642 DOI:10.3894/JAMES.2010.2.5.
- 643 Mapes, B., S. Tulich, J. Lin, and P. Zuidema, 2006: The mesoscale convection life cycle:
644 Building block or prototype for large-scale tropical waves? *Dyn. Atmos. Oceans*, **42**, 3–29.
- 645 Miyakawa, T., Y. N. Takayabu, T. Nasuno, H. Miura, M. Satoh, and M. Moncrieff, 2011:
646 Convective momentum transport by rainbands within a Madden-Julian oscillation in a
647 global nonhydrostatic model with explicit deep convective processes. part I: Methodology
648 and general results. *J. Atmos. Sci.*, *accepted*.
- 649 Muller, C. J., L. E. Back, P. A. O’Gorman, and K. A. Emanuel, 2009: A model for the
650 relationship between tropical precipitation and column water vapor. *Geophys. Res. Lett.*,
651 **36**, ”L16 804, doi:10.1029/2009GL039 667”.
- 652 Murakami, T., 1980: Temporal variations of satellite-observed outgoing longwave radiation
653 over the winter monsoon region. Part I: long period (15-30 day) oscillations. *Mon. Wea.*
654 *Rev.*, **108**, 408–426.
- 655 Neelin, J. D., 1997: Implications of convective quasi-equilibrium for the large-scale flow.
656 *The Physics and Parameterization of Moist Atmospheric Convection*, R. K. Smith, Ed.,
657 Kluwer, 413–446.
- 658 Neelin, J. D. and I. M. Held, 1987: Modeling tropical convergence based on the moist static
659 energy budget. *Mon. Wea. Rev.*, **115**, 3–12.

- 660 Neelin, J. and J. Yu, 1994: Modes of tropical variability under convective adjustment and
661 the Madden-Julian Oscillation. Part I: Analytical theory. *J. Atmos. Sci.*, **51**, 1876–1894.
- 662 Neelin, J. D. and N. Zeng, 2000: A quasi-equilibrium tropical circulation model – formula-
663 tion. *J. Atmos. Sci.*, **57**, 1741–1766.
- 664 Neelin, J. D., I. M. Held, and K. H. Cook, 1987: Evaporation-wind feedback and low-
665 frequency variability in the tropical atmosphere. *J. Atmos. Sci.*, **44**, 2341–2348.
- 666 Neelin, J. D., O. Peters, and K. Hales, 2009: The transition to strong convection. *J. Atmos.*
667 *Sci.*, **66**, 2367–2384.
- 668 Pauluis, O., D. M. W. Frierson, and A. J. Majda, 2008: Precipitation fronts and the reflection
669 and transmission of tropical disturbances. *Q. J. R. Meteor. Soc.*, **134**, 913–930.
- 670 Peters, O. and J. D. Neelin, 2006: Critical phenomena in atmospheric precipitation. *Nature*
671 *Physics*, **2**, 393–396, doi:10.1038/nphys314.
- 672 Raymond, D. J., 2000: Thermodynamic control of tropical rainfall. *Quart. J. Roy. Meteor.*
673 *Soc.*, **126**, 889–898.
- 674 Raymond, D. J., 2001: A new model of the Madden-Julian Oscillation. *J. Atmos. Sci.*, **58**,
675 2807–2819.
- 676 Raymond, D. J. and Z. Fuchs, 2009: Moisture modes and the Madden-Julian Oscillation. *J.*
677 *Climate.*, **22**, 3031–3046.
- 678 Raymond, D. J., S. Sessions, A. H. Sobel, and Z. Fuchs, 2009: The mechanics of gross moist
679 stability. *J. Adv. Model. Earth Sys.*, **1**, doi:10.3894/JAMES.2009.1.9.
- 680 Roundy, P. E. and W. M. Frank, 2004: Effects of low-frequency wave interactions on in-
681 traseasonal oscillations. *J. Atmos. Sci.*, **61**, 3025–3040.

- 682 Sarachik, E. S. and M. A. Cane, 2010: *The El Niño - Southern Oscillation Phenomenon*.
683 Cambridge University Press, 369 pp.
- 684 Sessions, S., S. Sugaya, D. J. Raymond, and A. H. Sobel, 2010: Multiple equilibria in a
685 cloud-resolving model. *J. Geophys. Res.*, **115**, D12 110, doi:10.1029/2009JD013 376.
- 686 Sherwood, S. C., 1999: Convective precursors and predictability in the tropical western
687 Pacific. *Mon. Wea. Rev.*, **127**, 2977–2991.
- 688 Showman, A. P. and L. M. Polvani, 2010: The Matsuno-Gill model and equatorial superro-
689 tation. *Geophys. Res. Lett.*, **37**, L18 811, doi:10.1029/2010GL044 343.
- 690 Sobel, A. H. and C. S. Bretherton, 2003: Large-scale waves interacting with deep convection
691 in idealized mesoscale model simulations. *Tellus*, **55**, 45–60.
- 692 Sobel, A. H. and H. Gildor, 2003: A simple time-dependent model of SST hot spots. *J.*
693 *Climate*, **16**, 3978–3992.
- 694 Sobel, A. H., J. Nilsson, and L. M. Polvani, 2001: The weak temperature gradient approxi-
695 mation and balanced tropical moisture waves. *J. Atmos. Sci.*, **58**, 3650–3665.
- 696 Sobel, A. H., S. E. Yuter, C. Bretherton, and G. N. Kiladis, 2004: Large-scale meteorology
697 and deep convection during TRMM KWAJEX. *Mon. Wea. Rev.*, **132**, 422–444.
- 698 Sobel, A. H., G. Bellon, and J. Bacmeister, 2007: Multiple equilibria in a single-column model
699 of the tropical atmosphere. *Geophys. Res. Lett.*, **34**, L22 804,doi:10.1029/2007GL031 320.
- 700 Sobel, A. H., E. D. Maloney, G. Bellon, and D. M. Frierson, 2008: The role of surface fluxes
701 in tropical intraseasonal oscillations. *Nature Geosci.*, **1**, doi:10.1038/ngo312.
- 702 Sobel, A. H., E. D. Maloney, G. Bellon, and D. M. Frierson, 2010: Surface fluxes
703 and tropical intraseasonal variability: a reassessment. *J. Adv. Model. Earth Sys.*, **2**,
704 doi:10.3894/JAMES.2010.2.2.

- 705 Stechmann, S. N. and A. J. Majda, 2006: The structure of precipitation fronts for nite
706 relaxation time. *Theor. Comput. Fluid Dyn.*, **20**, 377–404.
- 707 Stevens, D. E. and R. S. Lindzen, 1978: Tropical Wave-CISK with a moisture budget and
708 cumulus friction. *J. Atmos. Sci.*, **35**, 940–961.
- 709 Su, H. and J. D. Neelin, 2002: Teleconnection mechanisms for tropical Pacific descent anoma-
710 lies during El Nino. *J. Atmos. Sci.*, **59**, 2694–2712.
- 711 Sugiyama, M., 2009a: Moisture mode in the tropics. Part I: Analysis based on the weak
712 temperature gradient approximation. *J. Atmos. Sci.*, **66**, 1507–1523.
- 713 Sugiyama, M., 2009b: Moisture mode in the tropics. Part II: Nonlinear behavior on an
714 equatorial β -plane. *J. Atmos. Sci.*, **66**, 1525–1542.
- 715 Tung, W.-W. and M. Yanai, 2002a: Convective momentum transport observed during the
716 TOGA-COARE IOP. Part I: General features. *J. Meteor. Soc. Japan*, **59**, 1857–1871.
- 717 Tung, W.-W. and M. Yanai, 2002b: Convective momentum transport observed during the
718 TOGA-COARE IOP. Part II: Case studies. *J. Meteor. Soc. Japan*, **59**, 2535–3549.
- 719 Waliser, D. E., K. M. Lau, and J. H. Kim, 1999: The influence of coupled sea surface
720 temperatures on the Madden-Julian oscillation: A model perturbation experiment. *J.*
721 *Atmos. Sci.*, **56**, 333–358.
- 722 Wang, B., 1988: Dynamics of tropical low-frequency waves: an analysis of the moist Kelvin
723 wave. *J. Atmos. Sci.*, **45**, 2051–2065.
- 724 Wheeler, M. and G. N. Kiladis, 1999: Convectively coupled equatorial waves: Analysis of
725 clouds and temperature in the wavenumber-frequency domain. *J. Atmos. Sci.*, **56**, 374–
726 399.
- 727 Zeng, N., J. D. Neelin, and C. Chou, 2000: A quasi-equilibrium tropical circulation model –
728 implementation and simulation. *J. Atmos. Sci.*, **57**, 1767–1796.

729 Zheng, Y., D. E. Waliser, W. F. Stern, and C. Jones, 2004: The role of coupled sea surface
730 temperatures in the simulation of the tropical intraseasonal oscillation. *J. Climate*, **17**,
731 4109–4134.

732 Zhu, H., H. H. Hendon, and C. Jakob, 2009: Convection in a parameterized and super-
733 parameterized model and its role in the representation of the MJO. *J. Atmos. Sci.*, **66**,
734 2796–2811.

735 Zurovac-Jevtic, D., S. Bony, and K. A. Emanuel, 2006: On the role of clouds and moisture
736 in tropical waves: A two-dimensional model study. *J. Atmos. Sci.*, **63**, 2140–2155.

737 **List of Tables**

738 1 Control values of model parameters. 34

TABLE 1. Control values of model parameters.

parameter	value	Definition
R_0	4.8mm d ⁻¹	Clear-sky radiative cooling
W_{max}	70 mm	Saturation column water vapor
P_R, a_d	8.22×10^{-5} mm d ⁻¹ , 15.6	constants in convective scheme
L	1500 km	length scale for wind response to precipitation
A	$0.8/L$ (m s ⁻¹)(mm d ⁻¹) ⁻¹ m ⁻¹	Magnitude of wind response to precipitation
k	2604 m ² s ⁻¹	diffusivity for moisture
U	5 m s ⁻¹	background low-level zonal wind
\tilde{M}	0.1	Normalized gross moist stability (when fixed)
r	0.1	Cloud-radiative feedback parameter
E_0, C_u	100 W m ⁻² , 7.5 W m ⁻³ s	Sfc. LH flux for $u = 0$, LH flux change per $ u $
W_0, τ_c	45 mm, 2.4 d	Background W and convective time scale for linear model

739 List of Figures

- 740 1 Daily surface latent heat flux, on the y -axis, vs. 850 hPa zonal wind, on the
741 x -axis, both quantities averaged from $0 - 20^\circ\text{S}$ at the longitude 141°E , from
742 the aqua-planet simulation of Maloney et al. (2010). The linear regression
743 line is also shown. 37
- 744 2 Growth rate (solid, d^{-1}) and phase speed (dot-dash, m s^{-1}) For the linear
745 model with a background value $W_0 = 45 \text{ mm}$ and a convective time scale
746 $\tau_c = 2.4 \text{ d}$. Here the wind shift $\delta = 0$ and the background wind is assumed
747 westerly, but the phase speed shown is that relative to the mean wind, rather
748 than relative to the surface. 38
- 749 3 Growth rate (d^{-1}) for the linear model with the same parameters as in Fig. 2,
750 except that on the left, the cloud-radiative feedback parameter r is varied
751 from 0 to 0.2 in increments of 0.05, and on the right the wind shift parameter
752 δ is varied from 0 to 500 km in increments of 100 km. Greater growth rate at
753 fixed wave number (for $k < 15$) occurs at greater r and greater δ ; the curves
754 with the maximum and minimum values of r are labeled on the plots. 39
- 755 4 Growth rate (left, d^{-1}) and phase speed (right, m s^{-1}) for the uncoupled linear
756 model with the same parameters as in Fig. 2, except that the background
757 column water vapor W_0 is varied from 40 to 65 mm in increments of 5 mm; the
758 saturation value is 70 mm. The inverse of the resulting linearized convective
759 time scale, τ_c^{-1} , is shown by the pluses on the left; τ_c itself varies from 7.3
760 to 0.03d. Smaller τ_c (larger W_0) corresponds to larger growth rate and larger
761 westward (more negative) phase speed; the curves with the maximum and
762 minimum values of W_0 are labeled on the plots. 40

763	5	Hovmoeller plots of saturation fraction W/W_{max} in integration with $\delta =$	
764		400, 0, -400 km (left, middle, right), other parameters as in table 1. The	
765		x axes show longitudinal distance in units of 10,000 km while the y axes show	
766		time in days (with the first day being day 321 of each integration). The dashed	
767		line in the left panel shows the basic flow speed, 5 m s^{-1} .	41
768	6	Results from integration with $\delta = 400$ km, other parameters as in table 1.	
769		Both panels show snapshots at day 321 of perturbation zonal wind and pre-	
770		cipitation (left, m s^{-1} and mm d^{-1}), and water vapor path and surface latent	
771		heat flux (right, mm and mm d^{-1}).	42
772	7	As in Fig. 6, but for $\delta = 0$.	43
773	8	As in Fig. 6, but for $\delta = -400$ km.	44
774	9	As in Fig. 5, but with $\delta = 400$ km and the radiative feedback parameter	
775		$r = 0.15$.	45

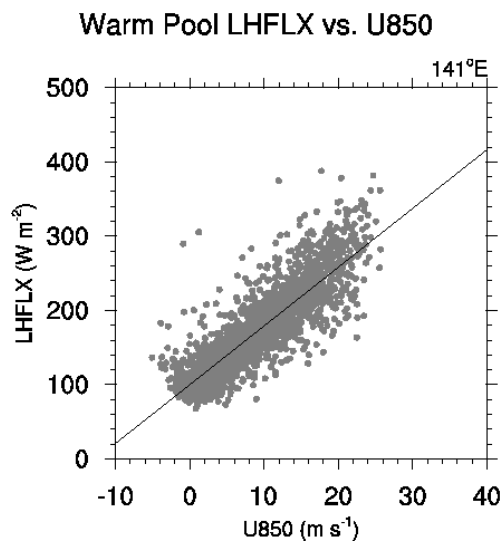


FIG. 1. Daily surface latent heat flux, on the y -axis, vs. 850 hPa zonal wind, on the x -axis, both quantities averaged from $0 - 20^\circ\text{S}$ at the longitude 141°E , from the aqua-planet simulation of Maloney et al. (2010). The linear regression line is also shown.

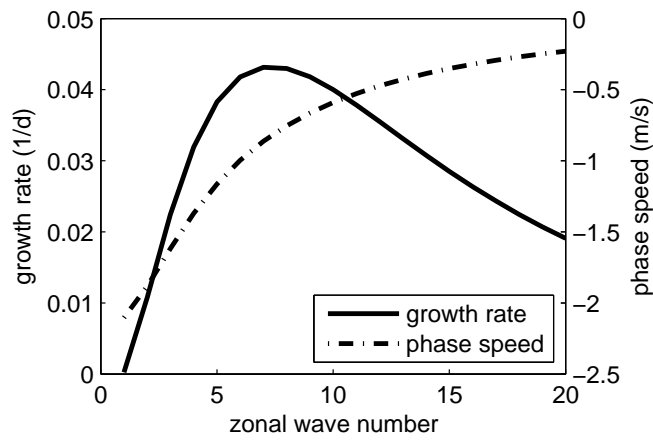


FIG. 2. Growth rate (solid, d^{-1}) and phase speed (dot-dash, m s^{-1}) For the linear model with a background value $W_0 = 45 \text{ mm}$ and a convective time scale $\tau_c = 2.4 \text{ d}$. Here the wind shift $\delta = 0$ and the background wind is assumed westerly, but the phase speed shown is that relative to the mean wind, rather than relative to the surface.

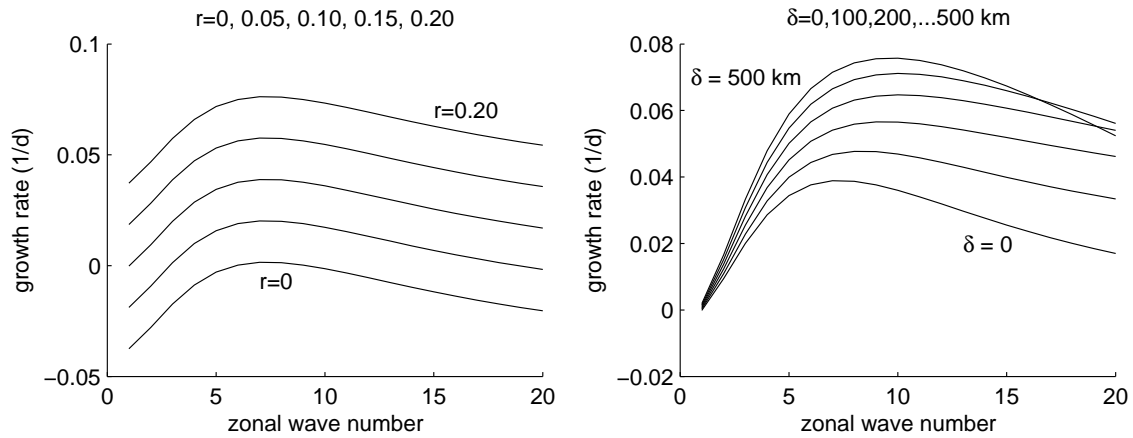


FIG. 3. Growth rate (d^{-1}) for the linear model with the same parameters as in Fig. 2, except that on the left, the cloud-radiative feedback parameter r is varied from 0 to 0.2 in increments of 0.05, and on the right the wind shift parameter δ is varied from 0 to 500 km in increments of 100 km. Greater growth rate at fixed wave number (for $k < 15$) occurs at greater r and greater δ ; the curves with the maximum and minimum values of r are labeled on the plots.

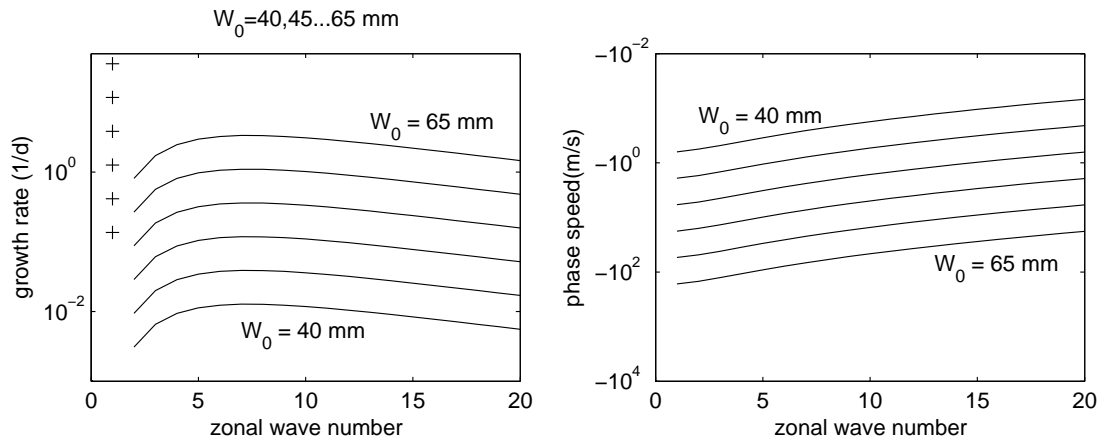


FIG. 4. Growth rate (left, d^{-1}) and phase speed (right, m s^{-1}) for the uncoupled linear model with the same parameters as in Fig. 2, except that the background column water vapor W_0 is varied from 40 to 65 mm in increments of 5 mm; the saturation value is 70 mm. The inverse of the resulting linearized convective time scale, τ_c^{-1} , is shown by the pluses on the left; τ_c itself varies from 7.3 to 0.03d. Smaller τ_c (larger W_0) corresponds to larger growth rate and larger westward (more negative) phase speed; the curves with the maximum and minimum values of W_0 are labeled on the plots.

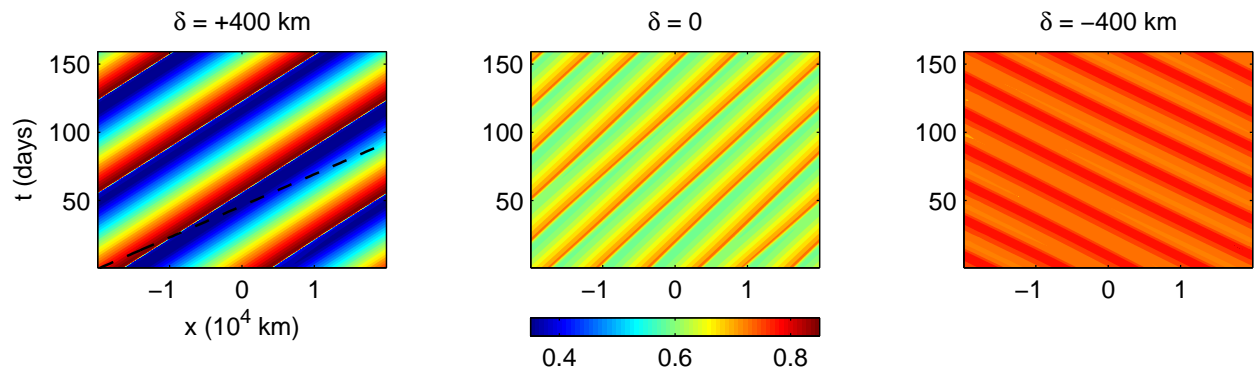


FIG. 5. Hovmoeller plots of saturation fraction W/W_{max} in integration with $\delta = 400, 0, -400$ km (left, middle, right), other parameters as in table 1. The x axes show longitudinal distance in units of 10,000 km while the y axes show time in days. The first day shown is day 321 of each integration, with the time values shown on the y axes corresponding to time since then. The dashed line in the left panel shows the basic flow speed, 5 m s^{-1} .

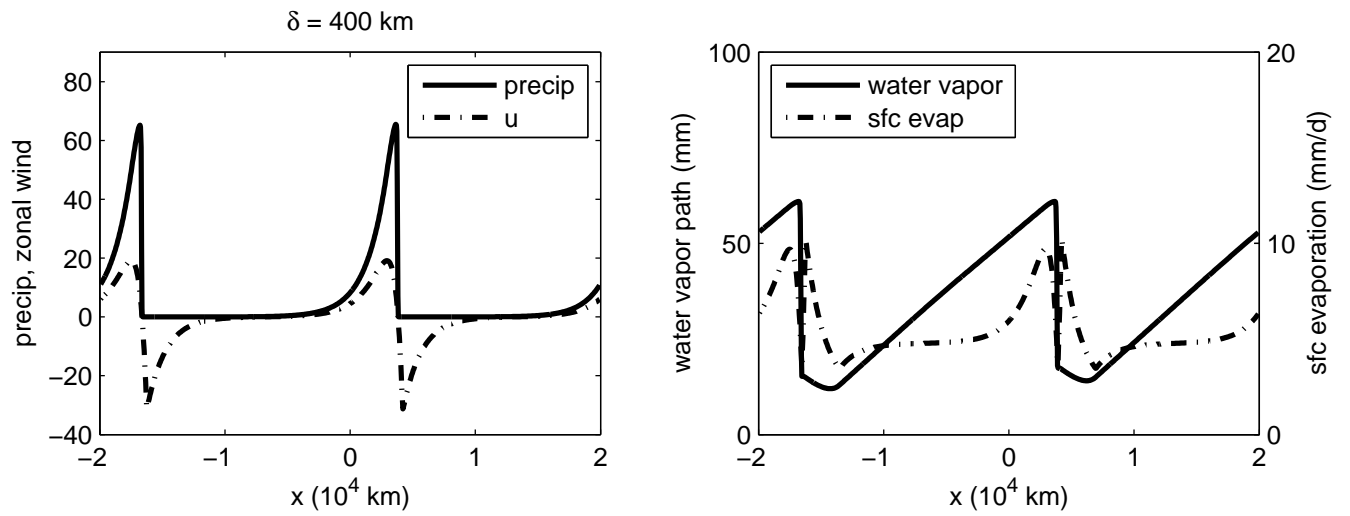


FIG. 6. Results from integration with $\delta = 400$ km, other parameters as in table 1. Both panels show snapshots at day 321 of perturbation zonal wind and precipitation (left, $m s^{-1}$ and $mm d^{-1}$), and water vapor path and surface latent heat flux (right, mm and $mm d^{-1}$).

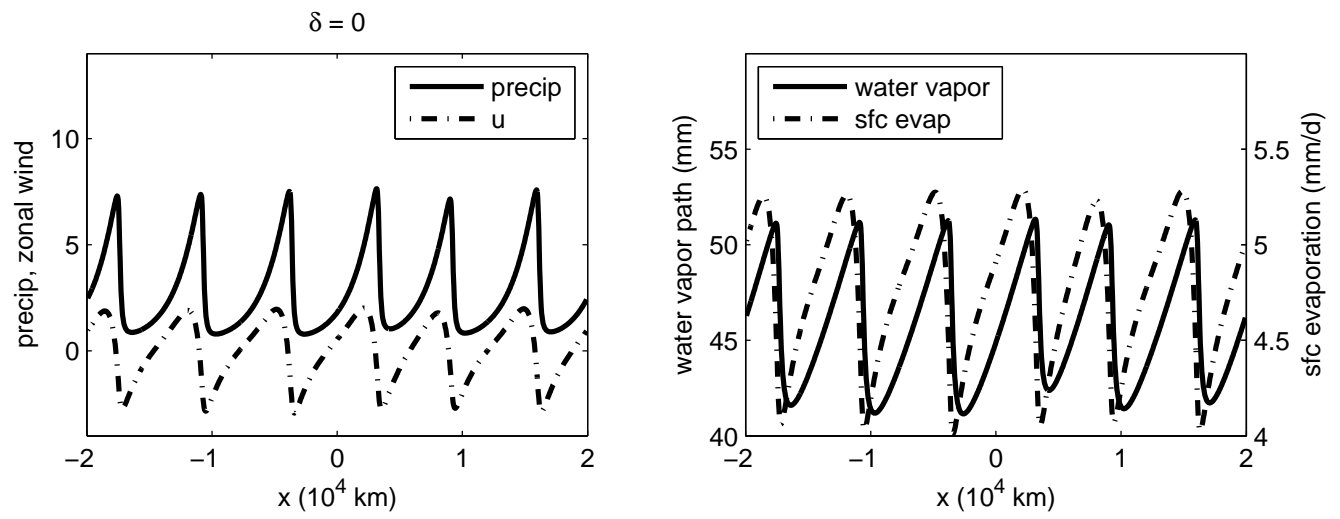


FIG. 7. As in Fig. 6, but for $\delta = 0$.

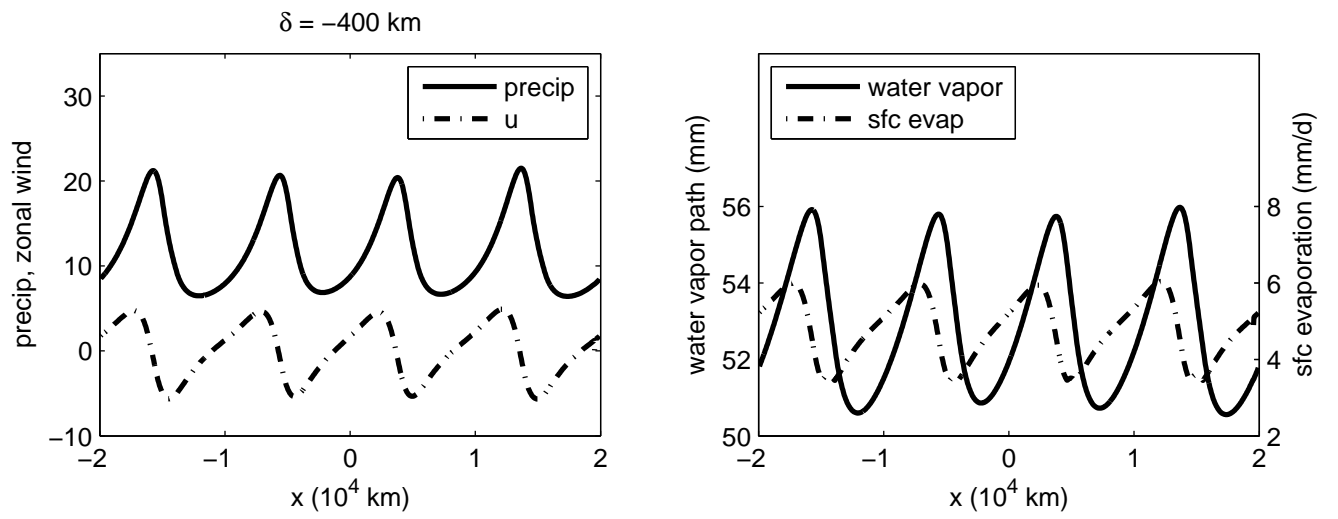


FIG. 8. As in Fig. 6, but for $\delta = -400$ km.

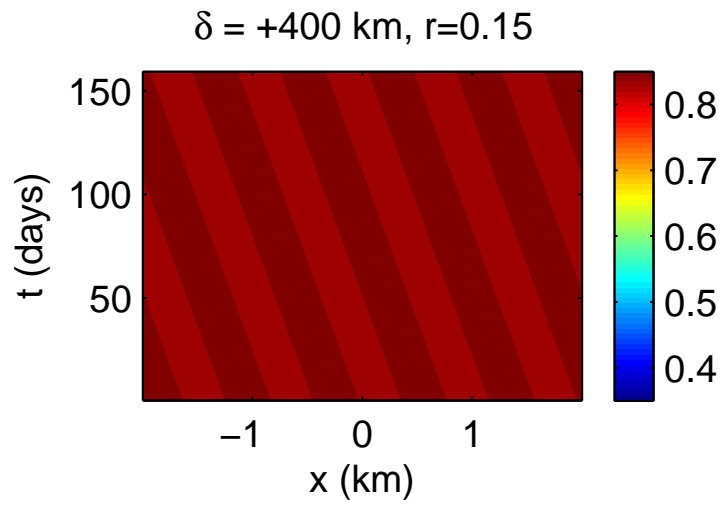


FIG. 9. As in Fig. 5, but with $\delta = 400 \text{ km}$ and the radiative feedback parameter $r = 0.15$.